

**PCCP**

Thermodynamic versus Non-Equilibrium Stability of Palmitic Acid Monolayers in Calcium-Enriched Sea Spray Aerosol Proxy Systems

Journal:	<i>Physical Chemistry Chemical Physics</i>
Manuscript ID	CP-ART-02-2018-001188.R1
Article Type:	Paper
Date Submitted by the Author:	04-Apr-2018
Complete List of Authors:	Wellen Rudd, Bethany; The Ohio State University, Department of Chemistry and Biochemistry Vidalis, Andrew; The Ohio State University, Department of Chemistry and Biochemistry Allen, Heather; The Ohio State University, Department of Chemistry and Biochemistry

SCHOLARONE™
Manuscripts

Thermodynamic versus Non-Equilibrium Stability of Palmitic Acid Monolayers in Calcium-Enriched Sea Spray Aerosol Proxy Systems

Bethany A. Wellen Rudd, Andrew S. Vidalis, and Heather C. Allen

Department of Chemistry & Biochemistry, The Ohio State University, Columbus, Ohio 43210, United States.

Abstract

Of the major cations in seawater (Na^+ , Mg^{2+} , Ca^{2+} , K^+), Ca^{2+} is found to be the most enriched in fine sea spray aerosols (SSA). In this work, we investigate the binding of Ca^{2+} to the carboxylic acid headgroup of palmitic acid (PA), a marine-abundant fatty acid, and the impact such binding has on the stability of PA monolayers in both equilibrium and non-equilibrium systems. A range of Ca^{2+} conditions from 10 μM to 300 mM was utilized to represent the relative concentration of Ca^{2+} in high and low relative humidity aerosol environments. The CO_2^- stretching modes of PA detected by surface-sensitive infrared reflection-absorption spectroscopy (IRRAS) reveal ionic binding motifs of the Ca^{2+} ion to the carboxylate group with varying degrees of hydration. Surface tensiometry was used to determine the thermodynamic equilibrium spreading pressure (ESP) of PA on the various aqueous CaCl_2 subphases. Up to concentrations of 1 mM Ca^{2+} , each system reached equilibrium, and Ca^{2+} :PA surface complexation gave rise to a lower energy state revealed by elevated surface pressures relative to water. We show that PA films are not thermodynamically stable at marine aerosol-relevant Ca^{2+} concentrations ($[\text{Ca}^{2+}] \geq 10 \text{ mM}$). IRRAS and vibrational sum frequency generation (VSFG) spectroscopy were used to investigate the surface presence of PA on high concentration Ca^{2+} aqueous subphases. Non-equilibrium relaxation (NER) experiments were also conducted and monitored by Brewster angle microscopy (BAM) to determine the effect of the Ca^{2+} ions on PA stability. At high surface pressures, the

relaxation mechanisms of PA varied among the systems and were dependent on Ca^{2+} concentration.

Keywords

Palmitic acid, calcium, monolayer, equilibrium spreading pressure, monolayer relaxation, stability, sea spray aerosols

Introduction

Aerosols and clouds constitute the largest uncertainty in the prediction of global climate change.¹ As approximately 71% of the earth is covered by water, marine sources contribute largely to the population of naturally produced aerosols.² By wind action on the ocean surface, sea spray aerosols (SSA) are generated and released to the neighboring atmosphere.³ The size and composition of SSA vary by their production method,^{4,5} and upon their generation, they transfer molecules and ions from the sea surface microlayer (SSML) to the aerosol phase.

The structure of organically enriched SSA can be described as an aqueous core surrounded by an organic layer of a complex mixture of surface active molecules, such as fatty acids.⁶⁻⁹ Of these fatty acids, those with chain lengths of sixteen and eighteen carbons are the most abundant, and the distribution of the fatty acids in the aerosol can vary with stages of biological activity.^{6,8,10} In both field and controlled laboratory studies, enrichment of Ca^{2+} ions, defined as the ratio of the concentration of Ca^{2+} relative to Na^+ ions in the aerosol phase and in bulk seawater (10 mM Ca^{2+} , 0.47 M Na^+), was observed for a range of aerosol sizes.¹¹⁻¹³ Additionally, calcium was found to be more enriched when compared to the other major seawater ions (K^+ , Mg^{2+} , Cl^- , SO_4^{2-}). Interestingly, the mechanism of calcium enrichment in the aerosol phase is not agreed upon. Jayarathne *et al*¹¹ and Cochran *et al*^{5,6} argue that the enrichment is due to the association of Ca^{2+} ions with organic complexing agents, and the

enrichment of the ion will depend on the production mechanism of SSA. However, Salter *et al*¹² posed a possible pathway to calcium enrichment via the formation of ionic clusters of carbonate at the water surface, without organic complexation. Their result suggests that organics may not drive ion enrichment, or are only required in small amounts.

Because the climate-relevant effects of SSA (light scattering, lifetime, reactivity, etc.) are influenced by their organic coatings,¹⁴⁻²⁰ the study of the impact of chemical complexity (i.e. ions, pH, mixtures) on monolayer properties is of importance. One way to evaluate monolayer stability is in terms of equilibrium spreading pressure (ESP), the thermodynamic equilibrium between 2D (monolayer) and 3D (bulk crystalline) states.²¹ In a recent review, it was pointed out that for many systems of atmospheric relevance, ESPs are not known,²² and that some surface tension-dependent models could actually use values of ESP to better understand film-forming organics on proxy droplets and particles.²³ The study of ESP may even extend past fundamental significance to describe real aerosol particles as it has been recently shown that complex 3D self-assembled phases form in aging model aerosol particles, which would increase the complexity of systems commonly modelled as monolayers alone.²⁴ Another evaluation of stability, monolayer relaxation, comes from interpreting changes in molecular area or surface pressure under mechanically-controlled conditions in a Langmuir trough, which is a non-equilibrium process.²⁵ Rarely though, are both techniques, ESP and non-equilibrium relaxation (NER), evaluated together for the same systems.

In this study we examine the effects of Ca^{2+} interactions with monolayers of palmitic acid (PA) at the air-aqueous interface as an idealized simple proxy system of SSA using a series of Ca^{2+} concentrations above and below 10 mM to represent calcium enrichment or depletion in the aerosol phase; Ca^{2+} enrichment in SSA may change as a function of the aerosol size and

environment based on relative humidity conditions (i.e. high humidity would lead to water uptake thereby diluting the Ca^{2+} concentration). Binding of the ion to the PA headgroup is studied with infrared reflection-absorption spectroscopy (IRRAS). Additionally, we utilize surface tension techniques and Brewster angle microscopy (BAM) to investigate the effect that such binding has on the stability properties of the monolayers, in both equilibrium and non-equilibrium systems, through the determination of ESPs and constant-surface pressure NER mechanisms. IRRAS and vibrational sum frequency generation (VSFG) spectroscopy are used to investigate the surface presence of PA molecules during ESP measurements at high Ca^{2+} concentration. We also discuss the cautions that must be exercised when interpreting monolayer stability in non-equilibrium systems. Through this work, the driving force of Ca^{2+} enrichment in the aerosol phase via binding, and the consequences of such enrichment on the stability of organic films at the aerosol-atmosphere interface are revealed.

Experimental Methods

Materials

Solid crystals of palmitic acid (PA, >99%, Sigma Aldrich) were used as received for the ESP measurements, and solutions of PA were prepared in chloroform (HPLC grade, Fisher Scientific) to a concentration of approximately 2 mM for monolayer NER experiments. Deuterated palmitic acid (d_{31} -PA) (>98%, Cambridge Isotopes Laboratories) was dissolved in chloroform to prepare spreading solutions for IRRAS experiments. The CaCl_2 solutions were diluted from stock solutions prepared by dissolving calcium chloride dihydrate (ACS grade, Fisher Scientific) in ultrapure water (>18.0 $\text{M}\Omega\cdot\text{cm}$, Barnstead Nanopure Filtration System D4741). The stock solutions were purified by previously reported methods,²⁶ and titrated via the

Mohr technique to determine chloride concentration prior to dilution.²⁷ To rule out the possibility of trace metals in our CaCl₂ solutions, control studies were conducted to reveal that the addition of EDTA (to bind and remove possible trace metals) did not affect the deprotonation signatures of d₃₁-PA on 300 mM CaCl₂ solutions (Fig. S4). Solutions were prepared and equilibrated at room temperature. All experiments were conducted at 21 ± 1°C with a relative humidity of 27 ± 9%.

Equilibrium Spreading Pressure (ESP)

Surface pressure (Π), the difference in surface tension between the bare aqueous surface (γ_0) and the film-covered surface (γ), in the ESP experiments was measured by a filter-paper Wilhelmy plate (Whatman 41, ashless grade) in a Teflon Langmuir MiniMicro trough (Biolin Scientific, area 145 cm²).

$$\Pi = \gamma_0 - \gamma \quad (1)$$

After a thorough cleaning procedure of ethanol and nanopure water, the trough was filled with the subphase of interest. The surface was swept with two Delrin barriers to ensure cleanliness ($\Pi < 0.20$ mN/m) prior to the start of the experiment. Approximately 1-3 mg of ground PA crystals were sprinkled across the surface with a spatula, and the time evolution of the surface pressure was recorded. When possible, a finite value of ESP was taken as the surface pressure at which a change of ≤ 0.1 mN/m occurred over a period of 15 minutes.

Monolayer Non-Equilibrium Relaxation (NER) at Constant Surface Pressure

After verifying that the aqueous surface in the Langmuir trough was clean (as described previously), monolayers of PA were spread dropwise by a microliter syringe (50 μ L, Hamilton) on the subphase of interest. The monolayers were compressed by symmetric compression of the

trough barriers to a target surface pressure (5 mN/m or 25 mN/m), and were maintained at that surface pressure by continuous motion of the barriers at a maximum rate of forward/backward motion of 1 mm/min. The change in relative area (A/A_0) was then analyzed as a function of time.

Infrared Reflection-Absorption Spectroscopy (IRRAS)

A custom-built setup used for IRRAS measurements was placed in the chamber of an FTIR spectrometer (Spectrum 100, Perkin Elmer), and consists of two gold mirrors. The first mirror directs the incoming unpolarized IR beam to the sample surface at a 46° angle of incidence, relative to the surface normal. As the beam is reflected off the surface, it is directed to a liquid nitrogen-cooled MCT detector by the second gold mirror. IRRAS spectra are plotted as reflectance-absorbance, calculated via

$$RA = -\log\left(\frac{R}{R_0}\right), \quad (2)$$

where R_0 is the background spectrum collected off the bare aqueous surface prior to the spreading of the monolayer. Each spectrum is the result of coaveraging 300 scans over the full spectral range ($4000\text{-}450\text{ cm}^{-1}$) at a 4 cm^{-1} resolution. The spectra shown here have been baseline-subtracted by a third order polynomial and are the average of at least 3 individual spectra.

Vibrational Sum Frequency Generation (VSFG)

The visible-infrared broadband SFG system used here has been described previously in the literature,^{28,29} but will be briefly outlined here. The $\sim 4\text{ W}$ output of a Ti:sapphire regenerative amplifier (Spitfire Ace, Spectra Physics, 75-femtosecond pulse length) was split to produce visible and tunable IR beams. To produce the IR beam, half of this output was directed to an optical parametric amplifier (TOPAS-C, Light Conversion) coupled to a non-collinear difference

frequency generator (NDFG, Light Conversion). The remaining portion of the amplifier output, used as the visible beam, was directed to an etalon (SLS Optics) to create asymmetric picosecond pulses with a FWHM of 12 cm⁻¹. The IR (centered at 2900 cm⁻¹, 15 μJ, 68°) and visible (800 nm, 90 μJ, 52°) beams were incident in a co-propagating geometry and the reflected sum frequency signal was collected by a spectrometer (Spectra Pro-500i, Princeton Instruments, 1200 grooves/mm grating) and a liquid nitrogen-cooled CCD (Spec-10:400B, 1340×400 pixels, Princeton Instruments). To reduce cosmic radiation spikes in the spectra, only a portion of the pixel area (vertically binned) was utilized in the signal collection. Spectra were measured in *ssp* and *ppp* polarization combinations with 5-minute exposure times. All spectra were background-subtracted and normalized to the non-resonant profile of a z-cut quartz crystal. In this study, VSG spectra of the CH stretching region were used to calculate the orientation of the terminal methyl group of the hydrocarbon chains of PA, thereby determining the tilt angle of the PA molecules in the monolayer. This procedure is outlined in the Supporting Information.

Brewster Angle Microscopy (BAM)

Brewster angle microscopy was used to image the surface during monolayer NER at 25 mN/m. The custom-built BAM setup used here has been described previously in the literature.^{30,31} A HeNe laser (Model 30528, Research Electro-Optics) emits vertically-polarized light at a wavelength of 543 nm and at a maximum power of 0.5 mW. The emitted light is attenuated by a half wave plate (Ekspla) and then further filtered by a Glan prism (Ekspla) before impinging the sample surface at the Brewster angle of the subphase (i.e. $\theta_{B,water} \approx 53.1^\circ$). The reflected light is collected by a 10x infinity-corrected super-long working distance objective lens (CFI60 TU Plan EPI, Nikon) and then collimated by a tube lens (MXA22018, Nikon) onto a back-illuminated EM-CCD camera (DV887-BV, 512×512 active pixels, 16×16 μm pixel size,

Andor). Images were cropped from their original size of 8.2×8.2 mm to show only the most resolved portion. The lateral resolution of the BAM images is 1.3 μm.

Results and Discussion

Binding of Ca²⁺ to the Palmitic Acid Headgroup

To investigate the binding of Ca²⁺ ions to the carboxylic acid headgroup of PA, IRRAS spectra were collected of d₃₁-PA monolayers spread to a condensed phase in a Petri dish at a mean molecular area of 20.5 Å²/molecule. The resulting spectra are shown in Fig. 1a for Ca²⁺ concentrations of 0 to 1 mM, and Fig. 1b for concentrations of 10 to 300 mM. In this region, there are four vibrational modes associated with the palmitic acid headgroup. The C=O (1722 cm⁻¹) and C-OH (1280 cm⁻¹) stretches are indicative of a protonated headgroup at the interface, and the asymmetric (~1540 cm⁻¹) and symmetric (~1410 cm⁻¹) stretches (ν_{AS}, ν_S) of the CO₂⁻ group are markers of deprotonation. The large positive feature in the spectra at ~1650 cm⁻¹ is the water bending mode from the aqueous subphase and is the result of the change in the refractive index of water in this wavelength region.^{32,33} As to not obscure the signals from the headgroup, perdeuterated PA (δCD₂ 1089 cm⁻¹) was chosen for these experiments to remove the CH₂ scissoring mode (~1460-1470 cm⁻¹) from the spectral region.³⁴

From the spectra, it can be seen that Ca²⁺-induced deprotonation of the carboxylic acid headgroup is observable even at the very low concentrations in Fig. 1a. The C=O and CO₂⁻ asymmetric stretch modes are the best indicators of the protonation state of the lipid headgroups. As the concentration of Ca²⁺ increases, the intensity of the C=O mode decreases, and that of the CO₂⁻ asymmetric stretch increases, as shown in Fig. 1c. While the intensities of the C=O and CO₂⁻ modes shed light on the protonation state of the molecules at the interface, the frequencies

of the asymmetric and symmetric stretching modes of the CO_2^- group are used to reveal information on the binding motif of the Ca^{2+} ion to the carboxylate headgroup of PA. Although we have previously studied Ca^{2+} :PA binding with VSFG,^{35,36} spectra collected with IRRAS have the advantage that both the symmetric and the asymmetric modes can be observed and interpreted together. In Fig. 1d, the center frequencies of the asymmetric (blue squares) and symmetric (red circles) stretches of the CO_2^- group are shown for all concentrations of Ca^{2+} upon which deprotonation of PA was observed within our limits of detection.

In previous literature, the frequency difference of asymmetric and symmetric stretches ($\Delta\nu_{\text{AS-S}} = \nu_{\text{AS}} - \nu_{\text{S}}$) of metal-bound acetate CO_2^- modes was used to characterize the binding motif of ions to acetate groups in four main geometries: monodentate, ionic, chelating bidentate, and bridging bidentate.^{37,38} For all Ca^{2+} concentrations studied here, the value of $\Delta\nu_{\text{AS-S}}$ of the d_{31} -PA monolayers stays relatively constant at $\sim 132 \text{ cm}^{-1}$. This value would generally associate these systems with an ionic binding motif, however contributions due to other binding geometries are also possible within the uncertainty of the measurements, and the overlap in $\Delta\nu_{\text{AS-S}}$ assignments.^{39,40} While these empirical rules have been applied to monolayer systems in the past,^{41,42} they were originally stated based on data of anhydrous crystals and ill-defined solutions of aqueous acetates with transition metal ions. Since the development of these guidelines, not much has been postulated about the details on the specifics of the binding motifs.

The values of ν_{AS} range from $1534\text{-}1544 \text{ cm}^{-1}$ and those of ν_{S} range from $1403\text{-}1413 \text{ cm}^{-1}$, with both modes blue-shifting with increasing concentration of Ca^{2+} in the subphase. The increase in frequency could be attributed to a change in the force constant of the O-C-O stretch as Ca^{2+} ions bind to the carboxylate headgroup of PA, as well as a change in the local hydration environment of the ion bound to the carboxylate.⁴¹⁻⁴³ The higher frequencies of the CO_2^-

stretches observed in the more concentrated Ca^{2+} regime suggest a more dehydrated binding state. This has been previously observed with high concentrations of Ca^{2+} ions and phosphate lipid headgroups.⁴⁴ So while the frequency difference between the asymmetric and symmetric stretches, derived from the empirical rules established for the bulk and crystalline phase⁴⁵⁻⁴⁷, reveals an ionic binding motif for all concentrations, the level of hydration in that motif can vary with ion concentration as shown in Fig. 2.

Analysis of the CD_2 scissoring mode (δCD_2) allows for interpretation of the lattice packing structure (hexagonal, orthorhombic, triclinic) of the d_{31} -PA molecules at the interface.^{48,49} Fig. 1a-b shows this region of the spectra ($1080\text{-}1100\text{ cm}^{-1}$). At all CaCl_2 concentrations, the δCD_2 mode is located at 1089 cm^{-1} , indicating that the PA molecules are packed in a hexagonal arrangement. This has been observed elsewhere in literature for both experimental and theoretical simulations.^{29,50,51} As a change in frequency of the scissoring mode is not observed, the 2D lattice packing structure of PA monolayers is not affected by its interaction with Ca^{2+} ions.

Stability of Palmitic Acid on CaCl_2 Subphases

Equilibrium Spreading Pressure

Surface pressure time evolution curves of PA on subphases of $[\text{Ca}^{2+}] \leq 1\text{ mM}$ are shown in Fig. 3a. PA crystals are sprinkled on the surface, and spontaneous spreading of molecules from the 3D bulk crystals to a 2D film causes a rise in surface pressure to values greater than 0 mN/m. The surface pressure at which there exists a plateau in the time evolution curve represents the ESP, defined as the thermodynamic equilibrium between the 2D and 3D phases.²¹ The surface pressures at which these plateaus occur are shown in Table 1 and Fig. 3c. In this

concentration regime, it can be seen (Fig. 3a) that up to a concentration of 1 mM, the Ca^{2+} :PA monolayer systems reach an equilibrium state, and the binding of Ca^{2+} to PA gives rise to a lower energy surface revealed by the higher ESP relative to PA on pure water.

Previous results from the literature have shown that changes to the subphase, including the addition of salts, induce changes in ESP.^{29,52,53} Salts, including CaCl_2 , have a tendency to increase the surface tension of aqueous solutions relative to pure water.⁵⁴ One theory of ESP argued that ESP was a function of the surface tension of the bare liquid, the cohesion forces of the solid crystal at the interface, and the thickness of the surface layer.⁵⁵ Through this theory, assuming the cohesion of the solid is not affected by the liquid subphase, ESP would increase with increasing surface tension of the bare liquid.

While surface pressure elevation in surface adsorption isotherms can be attributed to higher concentrations of surfactant, the observed increase in ESP of the PA systems following salt addition can more appropriately be attributed to the effects of the Ca^{2+} ions on the organization of the film, and can be divided into two primary forces. The adhesion of the surface-active molecules to the subphase (force 1) would be increased upon the presence of salt due to the interaction between the polar carboxylic acid group of PA and the ions that lie just beneath the surface layer.⁵⁶⁻⁵⁸ In addition to the forces between the molecules and the subphase, the presence of Ca^{2+} ions in solution will also affect the forces between individual surfactant molecules at the interface (force 2). As observed in Fig. 1a, Ca^{2+} induces a small fraction of dissociation in the PA film at low concentrations (most noticeably at 1 mM concentration). Although it was not detected within the limits of detection by Tang *et al.* in their study of Ca^{2+} interaction with PA,³⁶ such ion-induced deprotonation can cause a change in the orientation of

the dissociated carboxylate groups, resulting in increased repulsive forces between the molecules and increased surface pressure.^{56,59,60}

The relative impact of a salt on the ESP of a film at the interface also partly depends on the energy of hydration of the influencing ion.⁵⁶ For example, we have previously shown that the addition of 100 mM NaCl to a fully protonated PA system will raise the ESP from 7.6 to 17.8 mN/m.²⁹ In the current study, it only required 1 mM CaCl₂ for PA to reach an ESP of 14.6 mN/m (from 7.5 mN/m for PA on pure water). The greater change induced by Ca²⁺ in raising the ESP of the PA system, in the low concentration regime, can be correlated to its larger energy of hydration (-1505 kJ/mol) versus that of Na⁺ (-365 kJ/mol).⁶¹ The energy of hydration is defined as the amount of energy released when one mole of the ion is dissolved in water to form an infinitely dilute solution.⁶¹ Additionally, according to the Laws of Matching Water Affinities, Ca²⁺ ions have been shown to be well-matched to carboxylates as they share similar hydration properties, and the complexes readily form inner sphere ion pairs.⁶² Such differences between divalent and monovalent interactions have been previously documented for ESP measurements as well as spectroscopic and molecular dynamics studies on ion binding to lipid headgroups at the interface.^{44,60,63-65}

Unlike the low concentration regime, at $[\text{Ca}^{2+}] \geq 10 \text{ mM}$, the ESP curves do not reach similar plateaus in surface pressure and their interpretation becomes more complicated. Fig. 3b shows the results for $10 \text{ mM} \leq [\text{Ca}^{2+}] \leq 300 \text{ mM}$, and rather than reaching an equilibrium state, all of these systems instead establish a metastable state followed by a surface pressure decline. The values for the metastable states and the rates of surface pressure decline (approximated by a linear fit) are shown in Table 2. The maximum surface pressure attained at the metastable state decreases with increasing concentration of Ca²⁺, and the rate of surface pressure decline

increases with concentration, indicating that the films become less thermodynamically stable with increasing Ca^{2+} concentration.

A previous study also examined the effect of Ca^{2+} on the ESP of palmitic acid films and revealed a similar trend to the data shown in Fig. 3.⁶⁶ In that study, the decline of the surface pressure versus time curves for PA on higher concentrations of CaCl_2 was attributed to the “disappearance” of the monolayer with time. Trapeznikov argued that this monolayer disappearance was due to molecules of calcium palmitate re-adsorbing to the 3D PA crystals, thus removing themselves from the 2D aqueous surface.⁶⁷ To test this theory of the surface pressure decline in the ESP measurements, we applied the use of IRRAS (surface-sensitive) and VSFG (surface-specific) spectroscopies to the PA system on 300 mM CaCl_2 (the most extreme case of surface pressure decline). If the monolayer were to “disappear” from the surface, then the CH stretching modes of the PA molecules should not be observed in surface-specific VSFG spectroscopic measurements of the air-aqueous interface, although, they could still potentially be seen with IRRAS.

IRRAS measurements were conducted during the course of an ESP experiment, where the background spectrum of the 300 mM CaCl_2 subphase prior to the addition of solid PA crystals was used as R_0 in eqn. (2). Spectra were acquired continuously as soon as the PA crystals were deposited to the surface. For reference, the points along the ESP curve at which the spectra were taken are shown in the inset of Fig. 4 as colored symbols corresponding to their IRRAS spectrum. The first spectrum, starting at one minute after crystal deposition, shows no signatures of PA at the interface.

While still at a surface pressure of 0 mN/m, the IRRAS spectrum acquired at 7.5 minutes begins to show the CH stretching modes of the PA hydrocarbon chains. There are two likely

reasons why the intensity of this spectrum is much lower than that of the third spectrum, also at 0 mN/m, at 13.5 minutes. The first could be the fact that each spectrum is the average of 300 individual scans, so it is possible that the molecules had not eluted from the crystals at the start of the scan, and therefore no modes were observed. Later in the acquisition period, PA molecules could have appeared in the 2D space and contributed to the signal. The average of the 300 scans would incorporate both of these periods, thus giving rise to the less intense modes. The other explanation could be that upon elution from the crystal surface, the 2D film resembles that of a spread PA monolayer into the gas-liquid condensed phase of an isotherm which also has surface pressures of 0 mN/m. At this stage of a surface pressure-area isotherm, large islands of PA are formed, around which there exists lipid-poor regions (Fig. S7c). The average spectrum of a surface comprised of lipid-rich and lipid-poor regions could also give rise to weaker intensities than that of a homogenous film. From the third spectrum through the end of the experiment, the intensity of the CH modes remains nearly unchanged.

While it is surface-sensitive, IRRAS has a probing depth that can detect signals from the bulk.⁶⁸ To gain further evidence that there is still some form of a PA monolayer at the interface, surface-specific VSFG measurements were also taken during the surface pressure decline period of PA on the 300 mM CaCl₂ subphase. These spectra are shown in the inset of Fig. 5 (enlarged in Fig. S8) for both *ssp* and *ppp* polarizations. The measurements of the CH stretching region (2800-3000 cm⁻¹) were acquired at intervals of 2 mN/m from the metastable state of the surface pressure versus time curve until the surface pressure reached 0 mN/m. From the spectra, it can be seen that the CH stretching modes are still observable at a surface pressure of 0 mN/m. As VSFG is surface-specific, the spectra collected with this method confirm the IRRAS interpretation that the PA monolayer remains at the surface. There is still a surface presence of the PA molecules,

even at a surface pressure of 0 mN/m. These results suggest that the previous theory of Trapeznikov is flawed; the monolayer does not disappear from the surface during the surface pressure decline.

Using the intensity ratio of the ν_{AS-CH_3} in *ppp* polarization to the ν_{S-CH_3} in *ssp* polarization, the orientation of the terminal methyl group, θ_{CH_3} , can be determined.^{28,69,70} The tilt angle of the hydrocarbon chains, relative to surface normal, can be calculated from the relation, $\theta_{tilt} = 37^\circ - \theta_{CH_3}$, assuming a nearly trans configuration of the C_3 axis.⁷¹ Within experimental error (including errors related to the laser system as well as those related to configurational differences in the monolayer systems upon changes in surface coverage), the alkyl chain orientation of the PA molecules does not significantly change during the course of the surface pressure decline (Fig. 5). This was expected as it has been previously shown, with VSFG, that at high concentrations of Ca^{2+} in the subphase, the conformational ordering of PA remains similar for all nonzero values of surface pressure during a pressure-area isotherm.³⁶ Although this is not inconsistent with the surface pressure decline, the result leaves open the possibility that changes in the orientation of the CO_2^- headgroup may contribute to the surface pressure change rather than changes in the conformational ordering of the tails.

Because we have spectroscopic evidence that the surface pressure decline of PA molecules on high concentration $CaCl_2$ subphases is not due to the disappearance of the monolayers, we must attribute this phenomenon to other mechanisms. One possible explanation is that a closely-packed condensed state at a high surface pressure is not favorable for the ionized lipid molecules of calcium palmitate. Upon reaching this metastable state, the molecules relax into a more favorable configuration. While this state can eventually produce surface pressures of 0 mN/m for greater Ca^{2+} concentrations, there is still some form of a monolayer present, as

evidenced by the CH stretching modes, even though it may not be complete (similar to the gas-liquid condensed phase of PA monolayers (Fig. S7c)). The formation of these monolayer islands could also contribute to the slight change and increased error in the monolayer tilt angle measurement in Fig. 5 as the PA molecules in these islands can orient in different directions.

Relaxation phenomena of monolayers to more favorable states have also been considered in constant area NER experiments where monolayers are mechanically compressed to a target surface pressure and are then allowed to relax, subsequently lowering the measured surface pressure.⁷² Thermodynamically, the process observed here could be described as a result of two steps. The first is the spontaneous spreading of the surfactant at the interface to reduce the free energy and decrease the surface tension ($\Delta\gamma < 0$, $\Delta G < 0$, $\Delta H < 0$).⁷³ This step would represent the period from time 0 to the metastable state. Then, as Ca^{2+} induces a charge in the PA molecules of the monolayer, a closely packed negatively charged system is no longer enthalpically favorable ($\Delta H > 0$), and the surface tension rises as a result ($\Delta\gamma > 0$, where $\Delta\gamma = \gamma_{\text{final}} - \gamma_{\text{metastable}}$).⁷⁴

An alternative theory for the surface pressure decline comes from an understanding of the various equilibria occurring during an ESP measurement. Recall that the definition of ESP is the surface pressure at which the 2D monolayer and 3D bulk crystal phases are at equilibrium. When a finite value is obtained, it suggests that the monolayer is stable against the loss of molecules to dissolution or evaporation, which are often neglected in ESP experiments.⁷⁵ The complete picture of the various equilibria during an ESP measurement includes those between the 2D monolayer, 3D crystals, aqueous bulk phase, and vapor phase. Due to the low vapor pressure of PA,⁷⁶ the evaporation of the molecules can be considered negligible. In the scenario of the $[\text{Ca}^{2+}] \geq 10$ mM subphases, where finite ESP values are not attained, the additional equilibrium between the 2D monolayer and the aqueous subphase should also be considered. At a fixed area, it has

been shown that increased concentrations of calcium can increase the surface tension (decreasing surface activity) of fatty acid systems by removing the fatty acid salt from the interface.⁷⁷ Recall that surface tension and surface pressure (which we report here) are inversely related (i.e. high surface tension correlates with low surface pressure). Additionally, the removal of metal ions from fatty acid salts via titration with EDTA has shown the reverse effect. When the metal ion is removed, the surface tension decreases (increasing surface activity).⁷⁸

The effect of additional equilibria on the measured surface pressure in the $[\text{Ca}^{2+}] \geq 10$ mM regime can be proposed to follow the consequences of Le Chatelier's principle as illustrated in the schematic of Fig. 6. If equilibrium is achieved at the metastable state corresponding to the maximum surface pressure, even if only for a brief amount of time, then any loss of material from the 2D monolayer into the aqueous phase via solubilization or precipitation of calcium palmitate must be counteracted by a shift in the equilibrium from the 3D crystal phase to the 2D phase. If the rate of loss of the 2D monolayer is greater than the rate required to re-establish the 3D/2D equilibrium, then the surface pressure will not be able to be maintained. As there would be a constant replenishment of the 2D state from elution of molecules from the 3D crystals, the CH stretching modes of the monolayer would inevitably be present in the surface spectroscopies discussed earlier, which is what is observed in Fig. 4 and 5.

Non-Equilibrium Mechanically-Controlled Monolayer Relaxation

While the ESP determines the thermodynamic stability of spontaneously formed monolayers at the air-aqueous interface, other techniques have also been used to interpret monolayer stability in non-equilibrium systems at the interface. NER measurements involve compression of a spread monolayer to a target surface pressure or mean molecular area, followed by the maintenance of that target while monitoring the change in mean molecular area or surface

pressure, respectively, with time. The change in the relative molecular area (A/A_0) with time has been shown to be useful in determining the relaxation mechanisms of monolayers at the air-water interface.⁷⁹⁻⁸¹ The three most common mechanisms attributed to monolayer NER are 1) structural rearrangement during which only a small percentage of area loss occurs, 2) the desorption of molecules from the interface into the bulk, and 3) the transformation of monolayer material into 3D collapse-type structures at the surface.²⁵ Here we have investigated the relative area response to constant surface pressures in systems of PA on water, 1 mM CaCl₂, and 300 mM CaCl₂ at 5 mN/m and 25 mN/m, which represent pressures above and below the ESP of the systems (when applicable). The chosen subphases represent PA systems with the lowest and highest ESP, and one with the most dramatic surface pressure decline after the establishment of a metastable state.

At a constant surface pressure of 5 mN/m, all systems exhibit minimal relative area loss (Fig. 7). This result was expected as 5 mN/m is below the ESP for all systems studied. After 60 minutes, the water and 1 mM systems each exhibit only a small ~1% area loss. PA on a 300 mM CaCl₂ reaches a relative area of 0.98 after 60 minutes. With such minimal area losses at this surface pressure, the relaxation of all these systems is attributed to minor structural reorganization of the molecules at the interface.⁵⁸ Interestingly, the majority of the area loss in the 300 mM CaCl₂ system occurs within the first 2 minutes. During these experiments, when the target surface pressure is reached, the compression barriers slow down to 20% of their rate during isotherm compression. Upon this break in the compression speed,⁷² the surface pressure of PA on 300 mM CaCl₂ drops from 5 mN/m to ~2.5 mN/m and the barriers must move further (thereby reducing the area) to accommodate for such a change in surface pressure (Fig. S9). Once the surface pressure of 5 mN/m is recovered, the system remains very stable over time.

The same experiments were conducted at a target surface pressure of 25 mN/m, and revealed differences in the stability of PA on the three subphases. Much like the 5 mN/m scenario, the relaxation of PA on the 300 mM CaCl₂ subphase (Fig. 8c) follows a mechanism of structural rearrangement with minimal area loss (~3% at 60 minutes). Similar results have been demonstrated in the literature for stearic acid monolayers on high salt concentration solutions.⁸⁰ The largest change in area for this system can, again, be attributed to the initial drop in surface pressure upon slowing of the compression barriers. Throughout the period of relaxation, no appreciable changes are observed in the BAM images of the homogeneous monolayer film.

The rapid area loss observed for PA on water at a constant surface pressure of 25 mN/m (Fig. 8a) is indicative of a collapse-type relaxation mechanism, and the NER curve was fit to the Vollhardt model of nucleation and growth (eqn. (3)).⁸² In this model, area loss of the monolayer system is attributed to the formation (instantaneous or progressive) of nucleation centers and the geometric growth (hemispherical or cylindrical) of these centers by the uptake of insoluble monolayer material on the air side of the interface.

$$\frac{A_0 - A}{A_0 - A_\infty} = 1 - e^{-K_x t^x} \quad (3)$$

In this equation, A is the molecular area at a particular time (t), A_0 is the initial molecular area, A_∞ is the molecular area at infinite time, and K_x is the overall transformation rate constant. The time exponent, x , is characteristic of the nucleation mechanism and is the parameter used to identify the mechanism based on a fit of the constant surface pressure relaxation data. There are four values of x (1.5, 2, 2.5, 3) which have been specified by Vollhardt's model, each of which corresponds to a different nucleation and growth mechanism.⁸³

While the values of A and A_0 are obtained directly from the experimental data, the value of A_∞ must be extrapolated from a fit of the NER curve.⁸⁴ Briefly, A/A_0 was plotted against the

reciprocal of time ($1/t$) and a linear line of best fit was used to fit the initial portion of the resulting curve (see Fig. S10 in the Supporting Information). At $t \rightarrow \infty$, the y-intercept of the line of best fit represents A_∞/A_0 , and from this, A_∞ can be determined. When fit to eqn. (3) (see Fig. S11), the characteristic parameter, x , was found to be 1.9 ± 0.2 . According to this value, at 25 mN/m, the relaxation of PA on a water subphase follows a mechanism of instantaneous nucleation with cylindrical edge growth ($x = 2$). This collapse-type relaxation mechanism can be visualized in the BAM images along the curve. Before the system reaches 25 mN/m during compression, small 3D aggregates are observed and can be seen in the BAM image at 0 minutes. As the system is maintained at 25 mN/m, the mechanism of nucleation and growth can be observed by the formation of large 3D aggregates. Some of these aggregates can take up a majority of the field of view of the BAM image.

Of the three systems tested, the relaxation of PA on water exhibited the greatest variability in the NER curves. This can be attributed to several factors. The first of these possible factors is how well the mechanically controlled system is able to maintain a constant surface pressure of 25 mN/m. In some cases, material loss via nucleation and growth may occur too rapidly for the system to reestablish the 25 mN/m surface pressure by the slow rate of the barriers during the mechanical relaxation period. This can be seen in Fig. S12 where two extreme cases are shown; one that maintains the target surface pressure, and another during which the surface pressure starts to decrease after only about 6 minutes of control. Upon fitting, the system which is better able to maintain the target surface pressure gave a greater value of the characteristic parameter, x , than the system which was unable to recover from the loss of material to maintain the same surface pressure. The causes for surface pressure instability in the controlled surface pressure systems are numerous, and one may never be able to definitively

assign such behavior to a single factor. Variables like small temperature and humidity fluctuations may impact the resulting stability or instability of the system.⁸⁵ Additionally, if dust particles, for example, land on the monolayer-covered surface, nucleation may be promoted more quickly than on a perfectly clean surface.

On the 1 mM CaCl₂ subphase, a different type of relaxation curve is observed from the other two systems (Fig. 8b). Here, PA experiences a relative area loss of ~10% after 100 minutes and exhibits a different shape than the relaxation curves obtained on 300 mM CaCl₂ or on water. BAM images are more similar to those of the 300 mM CaCl₂ system and do not change appreciably with time. The concave-up decay shape of the PA NER curve on this subphase would generally be fit to a two-step desorption mechanism (eqn. (4)).⁸⁶ The first step, dissolution ($K_1t^{1/2}$), describes the transfer of molecules from the monolayer into a subsurface region. After some time, this subsurface becomes saturated and molecules begin the process of diffusion (K_2t) into the bulk. K_1 and K_2 are the rate constants associated with the dissolution and diffusion processes, respectively.

$$\ln\left(\frac{A}{A_0}\right) = K_1t^{1/2} + K_2t \quad (4)$$

Due to nonlinearity in the 1 mM CaCl₂ data at small times plotted against $t^{1/2}$, an accurate fit to eqn. (4) cannot be obtained. When compared to other studies in the literature, this system exhibited minimal area loss than those experiments for which this fitting was successful.^{87,88}

While the system did not exhibit significant and rapid area loss, indicating a collapse-type mechanism, such mechanisms can certainly contribute to the observed area loss because the held surface pressure (25 mN/m) is above that of the ESP of PA on 1 mM CaCl₂ (14.6 mN/m), at which there is an equilibrium of the 2D monolayer and 3D bulk material (i.e. collapse structures). Therefore, multiple loss mechanisms must be considered in the interpretation of the

NER phenomena. To account for the possibility of monolayer collapse as a contributing factor to the observed area loss, we developed a new equation (eqn. (5)) to account for the possibility of both collapse and desorption.

$$\ln\left(\frac{A}{A_0}\right) = \ln\left(\left(1 - \frac{A_0 - A_\infty}{A_0}\right) + \left(\frac{A_0 - A_\infty}{A_0}\right)e^{-K_x t^x}\right) + K_1 t^{1/2} + K_2 t \quad (5)$$

This function is composed of the natural log of the Vollhardt equation (eqn. (3)), to capture loss due to collapse, and the dissolution and diffusion terms from eqn. (4). When applied to the NER curves of PA on 1 mM CaCl₂ (Fig. S13), there is excellent agreement ($R^2 > 0.99$) between the experimental data and eqn. (5). The values for the fitting parameters were found to be: $K_x = 0.010 \pm 0.003 \text{ min}^{-1}$ (overall collapse transformation rate constant; units depend on the value of x), $x = 1.1 \pm 0.1$ (nucleation and growth characteristic parameter), $K_1 = 0.0010 \pm 0.0005 \text{ min}^{-1/2}$ (dissolution rate constant), and $K_2 = 0.000078 \pm 0.000078 \text{ min}^{-1}$ (diffusion rate constant). From a reasonable fit to this equation, one can say that the NER of PA on 1 mM CaCl₂ is likely due to a combination of collapse and desorption mechanisms occurring at surface pressures above the ESP. Recall that, as shown in the IRRAS spectra of Fig. 1a, at a 1 mM CaCl₂ concentration in the subphase, there exists both protonated and Ca²⁺-bound deprotonated PA species in the monolayer. Such a mixed monolayer should experience a more complicated relaxation mechanism because the protonated and Ca²⁺-bound PA molecules individually exhibit vastly different mechanisms.⁸⁹

ESP vs. NER Stability

If one were to only examine monolayer NER at 25 mN/m to evaluate the stability of PA films on these three subphases, the conclusion would be that PA is the most stable on the 300 mM CaCl₂ subphase. However, from knowledge of the ESP measurements conducted in this

work, such a statement would be misleading. One must then ask why mechanically controlled, non-equilibrium monolayer relaxation gives a differing view of stability from ESP measurements. According to Gaines, at surface pressures above the monolayer stability limit, the surface pressure that is measured is the sum of two contributions: the thermodynamic term relating surface tensions ($\gamma_0 - \gamma$), and the pressure induced by the 2D compression forcing of the surfactant molecules together.²¹ In a system like PA on 300 mM CaCl₂, this second compression force likely dominates at all points along the compression isotherm up to and including the maintained surface pressure of 25 mN/m, and the entire system can be considered metastable.⁵⁸ Unlike ESP measurements, “stability” in a non-equilibrium system, such as monolayer relaxation, refers to the expulsion of material from the monolayer (collapse aggregates or dissolution), not the achievement of the thermodynamically favorable state. Such designations are quite important as one can interpret stability very differently between ESP and NER measurements, as shown here for the example PA systems on water, 1 mM, and 300 mM CaCl₂.

Conclusions

In this work, the binding of Ca²⁺ ions to the carboxylic acid headgroup of PA monolayers, and the effects of such binding on monolayer stability were evaluated with surface-sensitive spectroscopies, Brewster angle microscopy, and surface tensiometry techniques. From IRRAS spectra of the spread monolayers, it was found that the extent of deprotonation via Ca²⁺ binding became more prevalent with increasing concentration, but the 2D hexagonal lattice packing of the PA monolayers was independent of Ca²⁺ concentration. While the common marker for binding motif, $\Delta\nu_{AS-S}$, remained constant at approximately 132 cm⁻¹, indicating ionic binding, the extent of hydration within this complexation changes with concentration.

Langmuir compression monolayers are often used as proxies for the organic films at the interface of SSA to represent the various phases associated with 2D monolayer concentration. However, they are approximating different aerosol environments as both compression isotherms and relaxation measurements push molecules through non-equilibrium states. In this work, we investigated equilibrium systems with ESP measurements to model ambient conditions that are relatively constant where aerosol films may be allowed to partition and spread to favorable states. Conversely, we utilized mechanically-controlled monolayer NER methods to see how interfacial aerosol films would respond to non-equilibrium conditions, representing the possible conditions of more dynamic air masses.

The ESPs of PA exhibited two different trends in the low (≤ 1 mM) and high (≥ 10 mM) Ca^{2+} concentration regimes, representing proxies of calcium-depleted or -enriched aerosols in high and low relative humidity constant ambient environments, respectively. At Ca^{2+} concentrations below 10 mM, thermodynamic equilibrium was achieved via spontaneous monolayer formation, and the value ESP increased with Ca^{2+} concentration. At concentrations of 10 mM and greater, such an equilibrium was not obtained and upon reaching a metastable state, surface pressures decreased with time. This decrease is attributed to the relaxation of the monolayer into a more favorable state, and/or to the effects of removal of the 2D monolayer into the bulk aqueous phase. Although for the high concentration of 300 mM CaCl_2 , the surface pressure reached 0 mN/m, spectroscopic evidence revealed that there still exists a monolayer film at the interface.

Monolayer NER experiments conducted at mechanically-controlled surface pressures above and below the measured ESP values revealed that all monolayers of PA could be considered stable against material loss at low surface pressures, but the monolayer systems

exhibited different relaxation mechanisms at high surface pressures. On water, PA relaxed with significant area losses via a mechanism of nucleation and growth into large 3D collapse aggregates, but on 1 mM CaCl_2 the monolayer exhibited a more complex mechanism which likely contained both collapse and dissolution relaxation processes.

Interestingly, on 300 mM CaCl_2 , PA would be considered the most stable from a NER perspective. However, the ESP data reveals that this Ca^{2+} concentration produced the least thermodynamically stable PA system. This suggests that the stability against material loss exhibited in the non-equilibrium relaxation experiments on 300 mM CaCl_2 is likely a consequence of the mechanical compression force on the monolayer in the Langmuir trough. Therefore, ion-bound monolayer stability phenomena should be investigated with multiple techniques, representing equilibrium and non-equilibrium states, to be better understood.

The results presented here suggest that it is reasonable to assume that Ca^{2+} enrichment in SSA is linked to organic complexation. Additionally, the aerosol-atmosphere interface will be affected by the Ca^{2+} ions bound to lipid molecules, and water accumulation or loss (resulting in concentration ranges of Ca^{2+}) leads to changes in the thermodynamic and non-equilibrium stability of the interfacial organic film in both constant and dynamic ambient environments.

Conflict of Interest

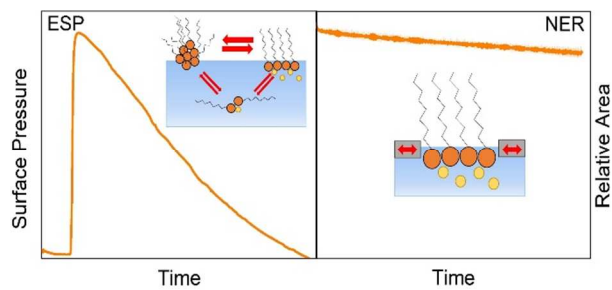
The authors declare no conflict of interest for this manuscript.

Acknowledgements

This research was supported under Grant CHE1305427 from the National Science Foundation via the Center for Aerosol Impacts on Chemistry of the Environment. The authors would like to

thank Dr. Lu Lin for assistance with the VSFG measurements.

Graphical Abstract



Calcium ions bind to palmitic acid monolayers at the air-aqueous interface resulting in changes of both thermodynamic and non-equilibrium stability.

Figures

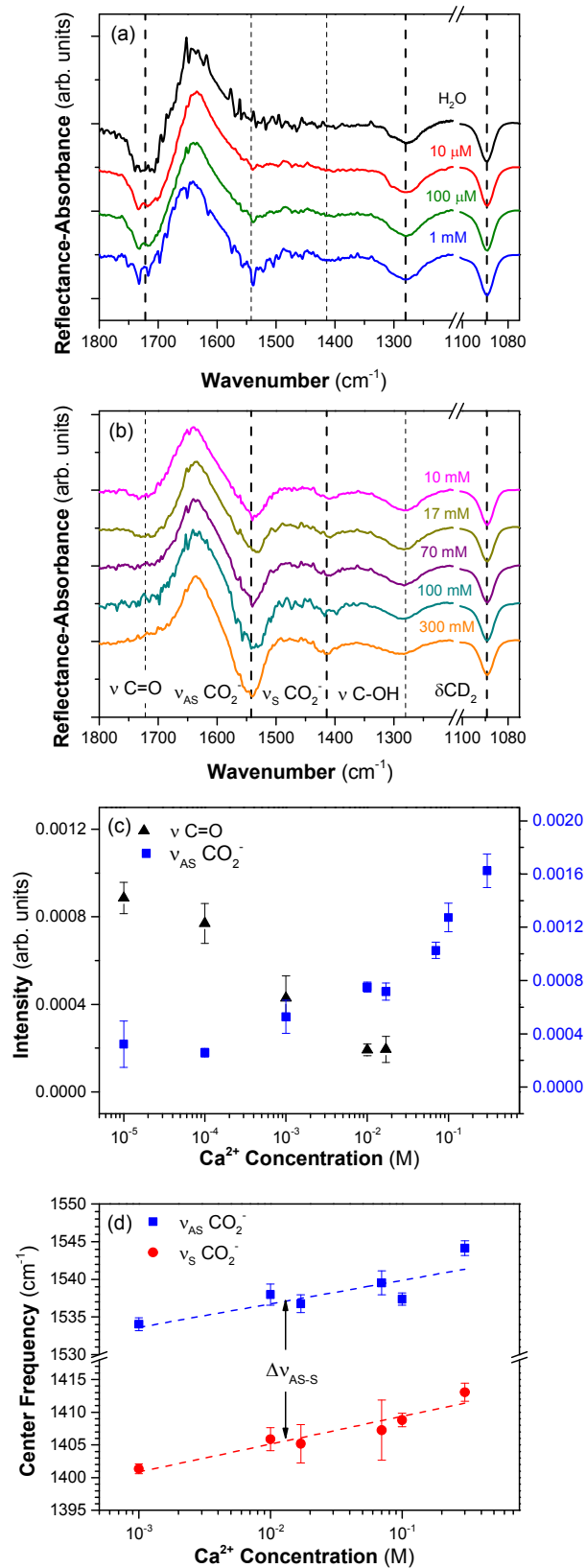


Fig. 1. IRRAS spectra of d_{31} -PA monolayers ($20.5 \text{ \AA}^2/\text{molecule}$) on CaCl_2 subphases of (a) low Ca^{2+} concentration ($0 \leq [\text{Ca}^{2+}] \leq 1 \text{ mM}$) and (b) high Ca^{2+} concentration ($10 \leq [\text{Ca}^{2+}] \leq 300 \text{ mM}$). Dashed lines are drawn to guide the eye at 1722 cm^{-1} ($\nu \text{ C=O}$), 1542 cm^{-1} ($\nu_{\text{AS}} \text{ CO}_2^-$), 1414 cm^{-1} ($\nu_{\text{S}} \text{ CO}_2^-$), 1280 cm^{-1} ($\nu \text{ C-OH}$), and 1089 cm^{-1} ($\delta \text{ CD}_2$). The intensities of the C=O (black triangles, left axis) and $\nu_{\text{AS}} \text{ CO}_2^-$ (blue squares, right axis) stretches as a function of Ca^{2+} concentration are shown in (c) with their respective axes, and are indicators of the protonation state of the PA molecules in the monolayer. In (d), the center frequency of the $\nu_{\text{as}} \text{ CO}_2^-$ (blue squares) and $\nu_{\text{s}} \text{ CO}_2^-$ (red circles) stretches are shown as a function of Ca^{2+} concentration in the aqueous subphase. The splitting of the CO_2^- modes ($\Delta\nu_{\text{AS-S}}$) is determined by taking the difference of the frequencies of the asymmetric and symmetric stretches, and is relatively constant with Ca^{2+} concentration. The intensities and frequencies in (c) and (d) are determined from Gaussian fits of the individual vibrational modes.

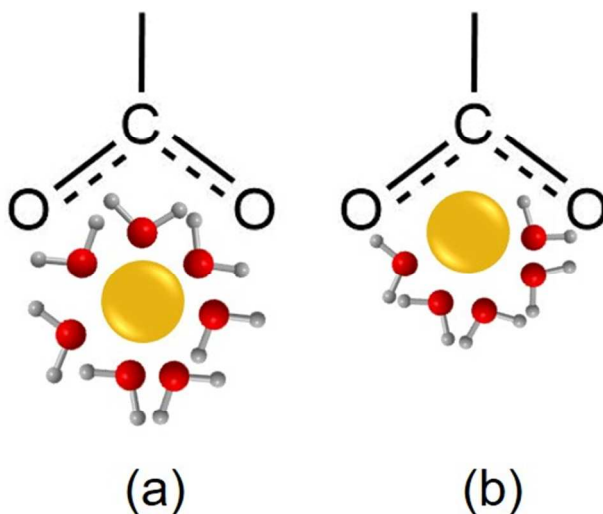


Fig. 2. Schematic of the ionic binding motif of a Ca^{2+} ion (yellow sphere) to the carboxylic acid headgroup of PA to illustrate (a) more and (b) less hydrated environments.

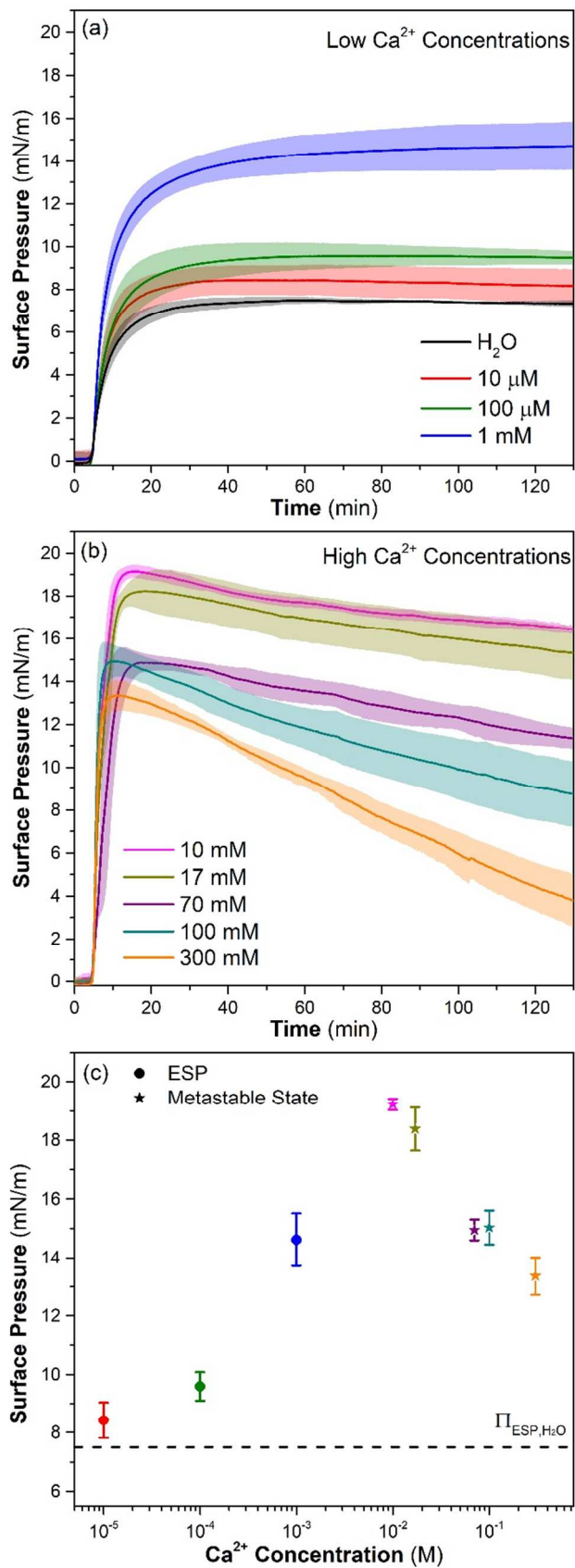


Fig. 3. Time evolution of surface pressure ESP curves of PA on CaCl_2 subphases of (a) low Ca^{2+} concentration ($0 \leq [\text{Ca}^{2+}] \leq 1 \text{ mM}$), and (b) high Ca^{2+} concentration ($10 \leq [\text{Ca}^{2+}] \leq 300 \text{ mM}$). Recall that oceanic $[\text{Ca}^{2+}]$ in bulk seawater is 10 mM. The time axis has been scaled such that the time prior to the surface pressure rise is constant among the trials (See Supporting Information Fig. S5). This time is not significant to the final ESP result, varies between experiments, and may be due to variations in the amount of crystals spread on the sample surface. The values of the ESP, or the maximum pressure metastable state, are shown in (c) as circles and stars, respectively, as a function of Ca^{2+} concentration. All curves and values represent the average of at least three individual trials. The shaded regions around the curves shown in (a) and (b), and the error bars in (c) represent \pm one standard deviation from the average.

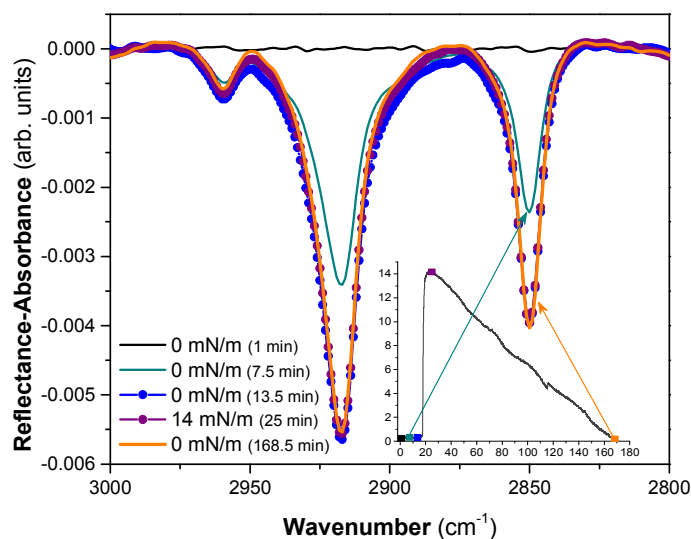


Fig. 4. IRRAS spectra in the CH stretching region of PA on 300 mM CaCl_2 during the course of the surface pressure decline of an ESP measurement. The intensity of the CH stretching modes remains largely unchanged despite the surface pressure decline. The inset shows the surface pressure vs. time ESP curve associated with the spectra (markers on the curve correspond to the colored spectra).

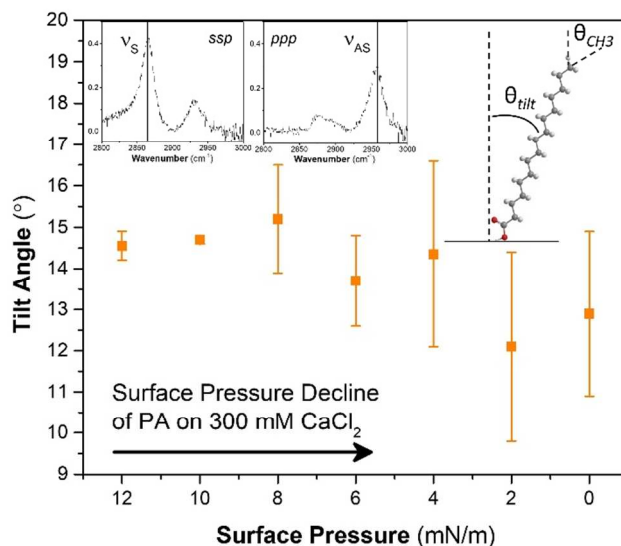


Fig. 5. Tilt angle of the PA chains as a function of surface pressure during the surface pressure decline of an ESP measurement of PA on 300 mM CaCl_2 . The tilt angle is calculated from the intensity of the symmetric (v_S) and asymmetric (v_{AS}) stretching modes of the CH_3 group in *ssp* and *ppp* polarizations, respectively. The inset shows the VSGF spectra for the 12 mN/m surface pressure for both polarization combinations. (see Fig. S8 for all spectra).

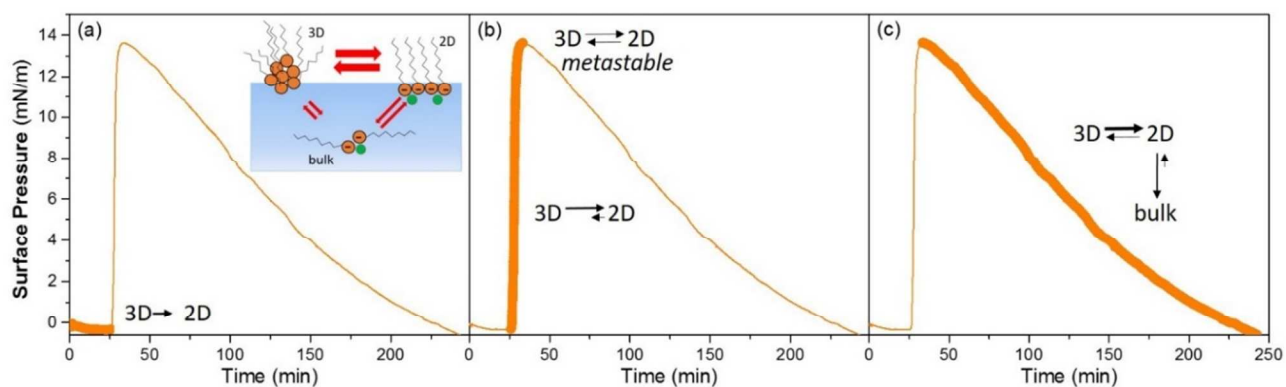


Fig. 6. Schematic of the proposed equilibria during an ESP experiment of PA on 300 mM CaCl_2 (equilibria to the vapor phase is omitted). The dominant equilibria are shown in each panel: (a)

elution of PA molecules from the 3D crystal into the 2D film, (b) continued elution of PA molecules from 3D to 2D film followed by a brief metastable state when equilibrium is established between the 2D and 3D states, (c) removal of the 2D calcium palmitate film into the bulk must be counteracted by a shift in the 3D/2D equilibrium toward the 2D monolayer.

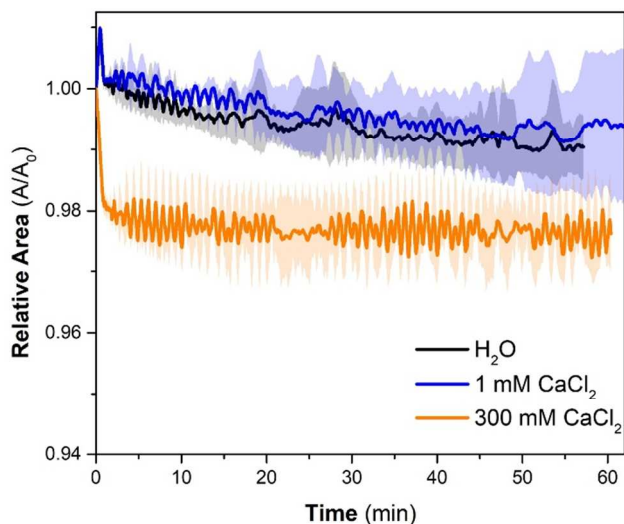


Fig. 7. Monolayer NER curves of PA maintained at a constant surface pressure of 5 mN/m on water (black), 1 mM CaCl₂ (blue), and 300 mM CaCl₂ (orange). Curves shown are the average of at least three measurements. The shaded regions around the curves represent \pm one standard deviation from the average of three trials.

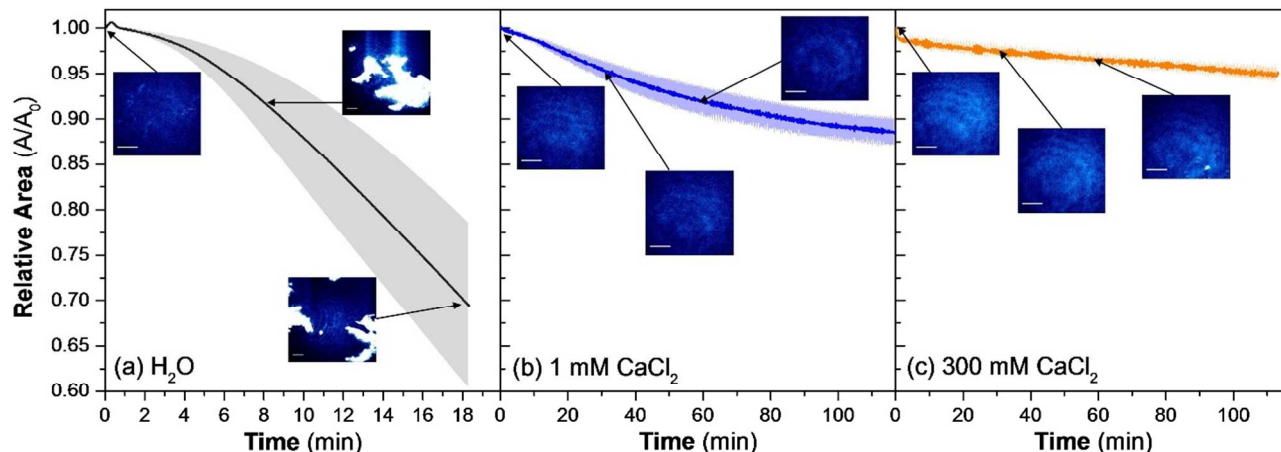


Fig. 8. Monolayer NER curves of PA maintained at a constant surface pressure of 25 mN/m on (a) water, (b) 1 mM CaCl_2 , and (c) 300 mM CaCl_2 . Curves shown are the average of at least three measurements. The shaded regions around the curves represent \pm one standard deviation from the average of at least three trials. BAM images are shown along the curves at the times at which they were captured during the relaxation process. All scale bars in BAM images represent a length of 100 μm . The surface morphology of PA on 1 mM and 300 mM CaCl_2 subphases remains homogeneous as a condensed film throughout the relaxation period. PA on water, however, exhibits a relaxation mechanism of nucleation and growth as evidenced by the large collapse structures. Because there is a limited field of view in BAM imaging, the time at which the large 3D structures are viewed for PA on water is not necessarily reproducible. The images in (a) are from multiple trials.

Tables

Table 1. Equilibrium spreading pressures of PA on CaCl_2 subphases up to 1 mM.

$[\text{Ca}^{2+}]$	ESP (mN/m)
0	7.5 ± 0.1
10 μM	8.4 ± 0.6
100 μM	9.6 ± 0.5
1 mM	14.6 ± 0.9

Table 2. Maximum surface pressure attained and the rate of surface pressure change after this metastable state during ESP measurements of PA on CaCl_2 subphases with concentrations of Ca^{2+} between 10 mM and 300 mM.

$[\text{Ca}^{2+}]$	Maximum Π (mN/m)	Change in Π ((mN/m)/min)
10 mM	19.2 ± 0.2	-0.013 ± 0.001
17 mM	18.4 ± 0.7	-0.014 ± 0.002
70 mM	15.0 ± 0.4	-0.030 ± 0.004
100 mM	15.0 ± 0.6	-0.040 ± 0.005
300 mM	13.4 ± 0.6	-0.069 ± 0.018

References

1. O. Boucher, D. Randall, P. Artaxo, C. Bretherton, G. Feingold, P. Forster, V.-M. Kerminen, Y. Kondo, H. Liao, U. Lohmann. Clouds and Aerosols. In: Stocker TF, Qin D, Plattner G-K, Tignor M, Allen SK, Boschung J, et al., editors. *Climate Change 2013: The Physical Science Basis. Contribution of Working Group I to the Fifth Assessment Report of the Intergovernmental Panel on Climate Change*. New York, NY, USA: Cambridge University Press; 2013.
2. B. J. Finlayson-Pitts, J. N. Pitts Jr., *Chemistry of the Upper and Lower Atmosphere*. Academic Press, San Diego, 2000.
3. R. S. Tseng, J. T. Viechnicki, R. A. Skop, J. W. Brown, *J. Geophys. Res.: Oceans*, 1992, **97**, 5201-5206.
4. D. C. Blanchard, L. D. Syzdek, *J. Geophys. Res.: Oceans*, 1988, **93**, 3649-3654.
5. R. E. Cochran, T. Jayarathne, E. A. Stone, V. H. Grassian, *J. Phys. Chem. Lett.*, 2016, **7**, 1692-1696.
6. R. E. Cochran, O. Laskina, T. Jayarathne, A. Laskin, J. Laskin, P. Lin, C. Sultana, C. Lee, K. A. Moore, C. D. Cappa, T. H. Bertram, K. A. Prather, V. H. Grassian, E. A. Stone, *Environ. Sci. Technol.*, 2016, **50**, 2477-2486.
7. G. B. Ellison, A. F. Tuck, V. Vaida, *J. Geophys. Res.: Atmos.*, 1999, **104**, 11633-11641.
8. M. Mochida, Y. Kitamori, K. Kawamura, Y. Nojiri, K. Suzuki, *J. Geophys. Res.: Atmos.*, 2002, **107**.
9. H. Tervahattu, K. Hartonen, V. M. Kerminen, K. Kupiainen, P. Aarnio, T. Koskentalo, A. F. Tuck, V. Vaida, *J. Geophys. Res.: Atmos.*, 2002, **107**.
10. R. E. Cochran, O. Laskina, J. V. Trueblood, A. D. Estillore, H. S. Morris, T. Jayarathne, C. M. Sultana, C. Lee, P. Lin, J. Laskin, A. Laskin, J. A. Dowling, Z. Qin, C. D. Cappa, T. H. Bertram, A. V. Tivanski, E. A. Stone, K. A. Prather, V. H. Grassian, *Chem*, 2017, **2**, 655-667.
11. T. Jayarathne, C. M. Sultana, C. Lee, F. Malfatti, J. L. Cox, M. A. Pendergraft, K. A. Moore, F. Azam, A. V. Tivanski, C. D. Cappa, T. H. Bertram, V. H. Grassian, K. A. Prather, E. A. Stone, *Environ. Sci. Technol.*, 2016, **50**, 11511-11520.
12. M. E. Salter, E. Hamacher-Barth, C. Leck, J. Werner, C. M. Johnson, I. Riipinen, E. D. Nilsson, P. Zieger, *Geophys. Res. Lett.*, 2016, **43**, 8277-8285.
13. F. J. Millero, *Chemical Oceanography*, 3rd ed. CRC Press, Boca Raton, 2006.
14. J. F. Davies, R. E. H. Miles, A. E. Haddrell, J. P. Reid, *Proc. Natl. Acad. Sci. U. S. A.*, 2013, **110**, 8807-8812.
15. W. D. Garrett, *J. Atmos. Sci.*, 1971, **28**, 816-&.
16. C. A. Randles, L. M. Russell, V. Ramaswamy, *Geophys. Res. Lett.*, 2004, **31**.
17. O. S. Ryder, N. R. Campbell, M. Shaloski, H. Al-Mashat, G. M. Nathanson, T. H. Bertram, *J. Phys. Chem. A*, 2015, **119**, 8519-8526.
18. M. A. Shaloski, T. B. Sobyra, G. M. Nathanson, *J. Phys. Chem. A*, 2015, **119**, 12357-12366.
19. L. F. Voss, M. F. Bazerbashi, C. P. Beekman, C. M. Hadad, H. C. Allen, *J. Geophys. Res.: Atmos.*, 2007, **112**.
20. A. A. Frossard, W. Li, V. Gérard, B. Nozière, R. C. Cohen, *Aerosol Sci. Technol.*, 2018, 1-11.
21. G. L. Gaines, *Insoluble monolayers at liquid-gas interfaces*. Interscience Publishers, 1966.

22. V. F. McNeill, N. Sareen, A. N. Schwier, *Top. Curr. Chem.*, 2014, **339**, 201-259.
23. W. Seidl, *Atmos. Environ.*, 2000, **34**, 4917-4932.
24. C. Pfrang, K. Rastogi, E. R. Cabrera-Martinez, A. M. Seddon, C. Dicko, A. Labrador, T. S. Plivelic, N. Cowieson, A. M. Squires, *Nat. Commun.*, 2017, **8**.
25. R. D. Smith, J. C. Berg, *J. Colloid Interface Sci.*, 1980, **74**, 273-286.
26. W. Hua, D. Verreault, E. M. Adams, Z. S. Huang, H. C. Allen, *J. Phys. Chem. C*, 2013, **117**, 19577-19585.
27. A. C. Finlayson, *J. Chem. Educ.*, 1992, **69**, 559-559.
28. E. M. Adams, D. Verreault, T. Jayarathne, R. E. Cochran, E. A. Stone, H. C. Allen, *Phys. Chem. Chem. Phys.*, 2016, **18**, 32345-32357.
29. E. M. Adams, B. A. Wellen, R. Thiriaux, S. K. Reddy, A. S. Vidalis, F. Paesani, H. C. Allen, *Phys. Chem. Chem. Phys.*, 2017, **19**, 10481-10490.
30. E. M. Adams, H. C. Allen, *Atmosphere*, 2013, **4**, 315-336.
31. C. B. Casper, D. Verreault, E. M. Adams, W. Hua, H. C. Allen, *J. Phys. Chem. B*, 2016, **120**, 2043-2052.
32. G. M. Hale, M. R. Querry, *Appl. Opt.*, 1973, **12**, 555-563.
33. E. Le Calvez, D. Blaudez, T. Buffeteau, B. Desbat, *Langmuir*, 2001, **17**, 670-674.
34. R. Mendelsohn, J. W. Brauner, A. Gericke, *Annu. Rev. Phys. Chem.*, 1995, **46**, 305-334.
35. C. Y. Tang, Z. S. Huang, H. C. Allen, *J. Phys. Chem. B*, 2011, **115**, 34-40.
36. C. Y. Tang, Z. S. A. Huang, H. C. Allen, *J. Phys. Chem. B*, 2010, **114**, 17068-17076.
37. G. B. Deacon, R. J. Phillips, *Coord. Chem. Rev.*, 1980, **33**, 227-250.
38. K. Nakamoto, J. Fujita, S. Tanaka, M. Kobayashi, *J. Am. Chem. Soc.*, 1957, **79**, 4904-4908.
39. J. E. Tackett, *Appl. Spectrosc.*, 1989, **43**, 483-489.
40. R. C. Mehrotra, R. Bohra, *Metal Carboxylates*. Academic Press, 1983.
41. A. Gericke, H. Huhnerfuss, *Thin Solid Films*, 1994, **245**, 74-82.
42. J. Simon Kutscher, A. Gericke, H. Huhnerfuss, *Langmuir*, 1996, **12**, 1027-1034.
43. D. J. Floisand, S. A. Corcelli, *J. Phys. Chem. Lett.*, 2015, **6**, 4012-4017.
44. E. M. Adams, C. B. Casper, H. C. Allen, *J. Colloid Interface Sci.*, 2016, **478**, 353-364.
45. J. W. DePalma, P. J. Kelleher, L. C. Tavares, M. A. Johnson, *J. Phys. Chem. Lett.*, 2017, **8**, 484-488.
46. D. A. Edwards, R. N. Hayward, *Can. J. Chem.*, 1968, **46**, 3443-&.
47. P. N. Nelson, R. A. Taylor, *Appl. Petrochem. Res.*, 2014, **4**, 253-285.
48. M. Boncheva, F. Damien, V. Normand, *Biochim. Biophys. Acta, Biomembr.*, 2008, **1778**, 1344-1355.
49. D. M. Small, *J. Lipid Res.*, 1984, **25**, 1490-1500.
50. A. Gericke, R. Mendelsohn, *Langmuir*, 1996, **12**, 758-762.
51. W. Lin, A. J. Clark, F. Paesani, *Langmuir*, 2015, **31**, 2147-2156.
52. B. J. Cheek, A. B. Steel, C. J. Miller, *Langmuir*, 2000, **16**, 10334-10339.
53. D. A. Knopf, S. M. Forrester, *J. Phys. Chem. A*, 2011, **115**, 5579-5591.
54. P. K. Weissenborn, R. J. Pugh, *J. Colloid Interface Sci.*, 1996, **184**, 550-563.
55. J. J. Bikerman, *Kolloid Z. Z. Polym.*, 1963, **191**, 33-&.
56. J. A. Donnison, E. Heymann, *Trans. Faraday Soc.*, 1946, **42**, 1-5.
57. J. N. Israelachvili, *Intermolecular and Surface Forces*. Academic Press, 2011.
58. E. Pezron, P. M. Claesson, J. M. Berg, D. Vollhardt, *J. Colloid Interface Sci.*, 1990, **138**, 245-254.

59. T. Zhang, S. L. Brantley, D. Verreault, R. Dhankani, S. A. Corcelli, H. C. Allen, *Langmuir*, 2017.
60. N. N. Casillas-Ituarte, X. Chen, H. Castada, H. C. Allen, *J. Phys. Chem. B*, 2010, **114**, 9485-9495.
61. Y. Marcus, *Biophys. Chem.*, 1994, **51**, 111-127.
62. K. D. Collins, *Biophys. Chem.*, 2006, **119**, 271-281.
63. A. Gilby, E. Heymann, *Aust. J. Chem.*, 1952, **5**, 160-172.
64. Y. Mao, Y. Du, X. Cang, J. Wang, Z. Chen, H. Yang, H. Jiang, *J. Phys. Chem. B*, 2013, **117**, 850-858.
65. T. Zhang, M. G. Cathcart, A. S. Vidalis, H. C. Allen, *Chem. Phys. Lipids*, 2016, **200**, 24-31.
66. A. A. Trapeznikov, *Proc. 2nd Intern. Congr. Surface Activity, London*, 1957, **1**, 109-120.
67. N. Pilpel, *Adv. Colloid. Interface Sci.*, 1969, **2**, 262-296.
68. E. C. Griffith, V. Vaida, *Proc. Natl. Acad. Sci. U. S. A.*, 2012, **109**, 15697-15701.
69. W. Gan, B.-h. Wu, Z. Zhang, Y. Guo, H.-f. Wang, *J. Phys. Chem. C*, 2007, **111**, 8716-8725.
70. H. F. Wang, W. Gan, R. Lu, Y. Rao, B. H. Wu, *Int. Rev. Phys. Chem.*, 2005, **24**, 191-256.
71. T. Nguyen, A. V. Nguyen, *Soft Matter*, 2014, **10**, 6556-6563.
72. M. I. Viseu, A. M. G. da Silva, S. M. B. Costa, *Langmuir*, 2001, **17**, 1529-1537.
73. A. M. Prpich, Y. B. Sheng, W. Wang, M. E. Biswas, P. Chen, *PLoS One*, 2009, **4**, e8281.
74. D. Hu, K. C. Chou, *J. Am. Chem. Soc.*, 2014, **136**, 15114-15117.
75. A. W. Snow, G. G. Jernigan, M. G. Ancona, *Thin Solid Films*, 2014, **556**, 475-484.
76. S. Chattopadhyay, P. J. Ziemann, *Aerosol Sci. Technol.*, 2005, **39**, 1085-1100.
77. D. Beneventi, B. Carre, A. Gandini, *J. Colloid Interface Sci.*, 2001, **237**, 142-144.
78. M. Sugawara, K. Isazawa, T. Kambara, *Fresenius Z. Anal. Chem.*, 1981, **308**, 17-20.
79. L. V. N. Avila, S. M. Saraiva, J. F. Oliveira, *Colloids Surf., A*, 1999, **154**, 209-217.
80. A. M. Brzozowska, M. H. G. Duits, F. Mugele, *Colloids Surf., A*, 2012, **407**, 38-48.
81. Y. L. Lee, J. Y. Lin, S. Lee, *Langmuir*, 2007, **23**, 2042-2051.
82. D. Vollhardt, U. Retter, S. Siegel, *Thin Solid Films*, 1991, **199**, 189-199.
83. D. Vollhardt, *Adv. Colloid. Interface Sci.*, 2006, **123**, 173-188.
84. Y. L. Lee, K. L. Liu, *Langmuir*, 2004, **20**, 3180-3187.
85. Z. Bilkadi, R. D. Neuman, *J. Colloid Interface Sci.*, 1981, **82**, 480-489.
86. L. Ter Minassian-Saraga, *J. Colloid Sci.*, 1956, **11**, 398-418.
87. J. M. R. Patino, M. R. R. Nino, *Colloids Surf., B*, 1999, **15**, 235-252.
88. C. C. Sanchez, M. R. Nino, J. M. R. Patino, *Colloids Surf., B*, 1999, **12**, 175-192.
89. P. Joos, M. Vanuffelen, *J. Colloid Interface Sci.*, 1993, **155**, 271-282.